Materials Research Bulletin 83 (2016) 615–622

Contents lists available at ScienceDirect

Materials Research Bulletin

journal homepage: www.elsevier.com/locate/matresbu

A study on the structural, electronic and optical properties of the α-AlF_3 compound

J.L. Navarro [a,b,*], E.A. Albanesi [a,b,**], R. Vidal [a,c], J. Ferrón [a,c]

[a] Instituto de Física del Litoral IFIS-Litoral-(CONICET-UNL), Güemes 3450, 3000 Santa Fe, Argentina
[b] Facultad de Ingeniería Universidad Nacional de Entre Ríos Oro Verde, Entre Ríos, Argentina
[c] Facultad de Ingeniería Quimica, Universidad Nacional de Litoral, Santa Fe, Argentina

ARTICLE INFO

Article history:
Received 16 March 2016
Received in revised form 29 June 2016
Accepted 7 July 2016
Available online 15 July 2016

Keywords:
Fluorides
Glasses
Optical material
Inorganic compounds
Electron energy loss spectroscopy
Electronic structure
Optical properties

ABSTRACT

The structural, electronic and optical properties of the insulator α-AlF_3 are investigated by first principles calculations using density functional theory, and the band gap and optical response is measured. Our calculations use the generalized gradient approximation for the exchange and correlation potential, within a pseudopotential scheme. In order to improve the ground state formulation for the electronic and optical properties, we included many body effects through the GW approximation for the band gap and the Bethe–Salpeter equation for the excitonic effects in the optical calculations. We contrast our calculations with experiments, by combining Ultraviolet and X-ray photoelectron spectroscopies on AlF_3 films grown over Cu(100) to determine the electronic structure, and electron energy loss spectra (EELS) to compare the optical spectra. The density of states shows the important role of F-p states in the bonding, and the band structure reveals the direct band gap at the Γ point of the material, with a value of 10.81 eV obtained within the GW approximation, in very good agreement with the experimental value of 10 eV. We also calculated the imaginary $\varepsilon_2(\omega)$ and real $\varepsilon_1(\omega)$ parts of the dielectric function, the refractive index, the extinction coefficient, the reflectivity at normal incidence, and the electron energy loss spectrum which is in reasonable agreement with the experimental curve, obtaining the main peak in the region about 25 eV. With the Bethe–Salpeter equation we calculated the energy loss spectra of the low energy region above the band gap, where we found excitonic effects that explain the observed experimental peak in this region.

© 2016 Elsevier Ltd. All rights reserved.

1. Introduction

The technological importance of group III–VII insulators compounds and their alloys have attracted the attention of many research groups in recent years. For example, aluminum fluoride have a great potential in catalysis, as support in reactions with other elements and because of its catalytic activity [1,2]; as an inorganic resist for nanometer scale patterning in electron beam lithography [3], to fabricate metallic nanowires by electron beam induced decomposition [4]; and in general as a support for nano and micro devices. AlF_3 is an III–VII ionic insulator that has a variety of polymorphisms [5,6] all of which convert in an irreversibly way to a stable phase known as α-AlF_3, within a temperature range between 730 and 920 K [7]. Chupas et al. [8] found that above the transition temperature of 730 K, α-AlF_3 has the cubic perovskite structure AMX_3 without the A element, where M is aluminum, surrounded by an octahedron of corner shared fluorine atoms (X). At lower temperatures, the structure becomes rhombohedral, and this symmetry can be described as a rotation of the fluorine octahedron about one of the threefold axis of the perovskite cubic cell [7]. Fig. 1 shows a schematic picture of the α-AlF_3 rhombhohedral crystal structure and its reciprocal lattice, with the lattice parameters [8] of $a = b = c = 5.03142$Å and angle $\alpha = 58.829°$. In the figure, Al atoms are represented in dark blue, while F atoms are represented in grey. This is a *XZ* plane view of the primitive rhombohedral cell, containing 8 atoms, 2 Al and 6 F atoms, organized like the R-3c structure, with the Al atoms surrounded by the F atoms.

* Corresponding author at: Instituto de Física del Litoral IFIS-Litoral-(CONICET-UNL), Güemes 3450, 3000 Santa Fe, Argentina.
** Principal corresponding author at: Instituto de Física del Litoral IFIS-Litoral-(CONICET-UNL), Güemes 3450, 3000 Santa Fe, Argentina.
E-mail addresses: jorge.navarro@ifis.santafe-conicet.gov.ar (J.L. Navarro), eduardo.albanesi@ifis.santafe-conicet.gov.ar (E.A. Albanesi), ricardo.vidal@ifis.santafe-conicet.gov.ar (R. Vidal), julio.ferron@ifis.santafe-conicet.gov.ar (J. Ferrón).

http://dx.doi.org/10.1016/j.materresbull.2016.07.007
0025-5408/© 2016 Elsevier Ltd. All rights reserved.

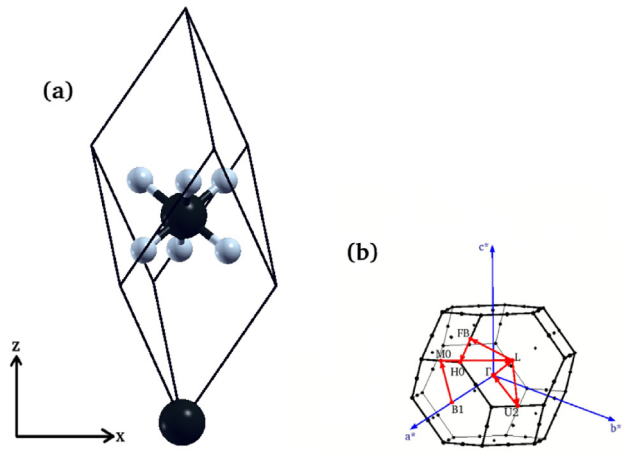

Fig. 1. (a) Direct primitive cell of the R-3c rhombohedral structure of α-AlF_3, showing the 8 atoms (dark blue: Al atoms), (grey: F atoms). (b) The rhombohedral first Brillouin zone (BZ), showing the *k*-point path (red lines) used in the band structure plot in Fig. 4. Both, the direct cell and the first BZ were obtained with the Xcrysden code [9] with the labels as in Ref. [10]. (For interpretation of reference to color in this figure legend, the reader is referred to the web version of this article.)

König et al. [5] made a spectroscopic characterization of the dielectric phases of AlF_3, using different techniques like X-ray diffraction (XRD) and nuclear magnetic resonance (NMR). Le Bail and Calvayrac [11] made a theoretical study analysing the hypothetic formation of several different AlF_3 crystal structures. On the other hand, the characterization of AlF_3 thin films or AlF_3 surfaces had been studied by different groups. For example, Wander et al. [1] studied the composition and structure of the α-AlF_3(0001) surface to show that the reactivity of the material depend on the surface termination. Moreno-López et al. [12] investigated, using scanning tunnel microscopy (STM), the first steps in the growth stage of the insulator-metal interface formed by α-AlF_3 deposited on Cu(100) surfaces at room temperature. Also theoretical studies [13] on the electronic properties of complex interfaces as $AlF_3/SiO_2/Si$ system have been performed.

The purpose of this work is to present experimental Ultraviolet (UPS), X-ray Photoelectron (XPS) and electron energy loss (EELS) spectroscopies, and band gap measurements, together with state of the art calculations on structural, electronic, and optical properties, including the EELS function of α-AlF_3.

2. Experimental setup

2.1. Surface and film growth characterization

The measurements reported in this paper have been performed in two different ultrahigh vacuum (UHV) chambers, equipped with a couple of common techniques in both of them in order to ensure the reproducibility of the experimental conditions. We combined Auger electron (AES), (UPS) and (XPS) spectroscopies to determine both; the quality of the AlF_3 film, as well as the interface, and the determination of the electronic structure, and loss spectra.

The AlF_3 was grown over a Cu(100) single-crystal, whose surface was cleaned by repeated cycles of Ar^+ sputtering (1 keV, ~5 μA cm^{-2}) and reconstructed by annealing at 800 K until contamination was below the detection limit of AES. AlF_3 (CERAC Inc, Milwaukee, WI, USA, 99.5% purity) was grown by thermal evaporation at deposition rates between 2×10^{-2} and 8×10^{-4} ML/s. The Knudsen cell had a thermocouple allowing us to monitor the crucible temperature, a shutter to precisely control the deposition time and a water-cooled shroud; the cell was carefully outgassed for several hours before starting the experiments at temperatures slightly above those used during growth. The pressure in the vacuum chambers was kept in the low 10^{-9} mbar range during evaporation, and fell into the mid 10^{-10} mbar range during the measurements. Depositions were done at room temperature.

We used electron beams of 2 keV for AES and 100 eV for EELS measurements; the incidence angle was 30° with respect to the surface normal in all cases. Particular care must be taken during measurements using electron bombardment, since it is well known that AlF_3 presents radiolysis, i.e. electron bombardment induces F detachment, leaving an Al^0 residue on the surface. This fact, very promising for electron lithography [3], is completely undesirable if we are interested in electron structure characterization. Thus, electron current density on the sample was kept low enough to minimize the effects of irradiation. Differentiated Auger spectra of the F_{KLL} and Al_{LVV} transitions and energy loss (EELS) spectra were acquired using a single-pass cylindrical mirror analyzer (CMA) with a resolution of 0.6% and 2V peak-to-peak modulation amplitude.

3. Results and discussion

3.1. AlF_3 growth and characterization

In Fig. 2 we summarize AES and XPS results for the AlF_3 film growth and the complete chemical characterization of the grown film (XPS). In the left graph we depict the Cu_{MVV}, F_{KLL} and Al_{LVV} Auger yields as a function of the evaporation time. The growth of the film is characterized by a decrease of the Cu signal and an increase of the Al and F Auger yields. The special characteristics of aluminum fluoride, known as radiolysis can be observed in this figure, i.e. the appearance of an Auger signal that corresponds to metallic aluminum. As we know, the electron bombardment produces the desorption of atomic Fluor and the appearance of reduced aluminum. This fact does not alter the sample, as a whole, as we see in the following, since the Al reduction is produced under the electron bombardment in a very small spot.

In the right column of Fig. 2 we show the XPS spectrum of the same sample. The figure shows the characteristics Auger (F_{KLL}) and photoelectron peaks (F1s and Al2s) that corresponds to F and Al. Additionally, we can see *O*1*s* and *C*1*s* peaks. These last peaks are the fingerprint of the contamination that takes place when the sample is translated from the growing to the characterization chamber.

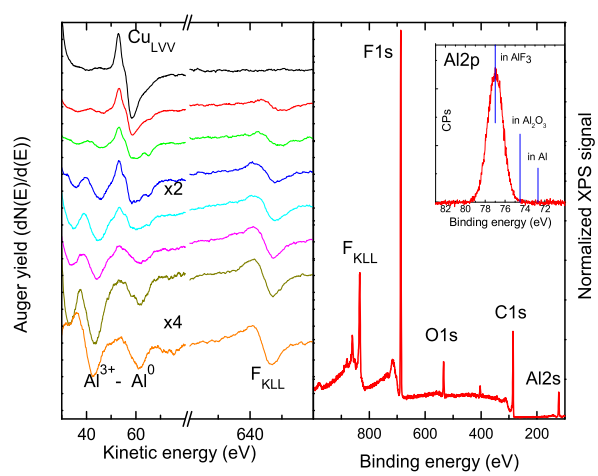

Fig. 2. Left: Growth of AlF_3 over Cu(001) followed by Auger electron spectroscopy. The top AES spectrum corresponds to pure Cu while the bottom spectrum to a thin AlF_3 film grown on Cu. Right: Wide band spectrum of AlF_3 thin film taken by X-ray photoelectron spectroscopy. Inset: XPS AL2p signal. Vertical bars identify Al in AlF_3, Al_2O_3 and metallic Al [14].

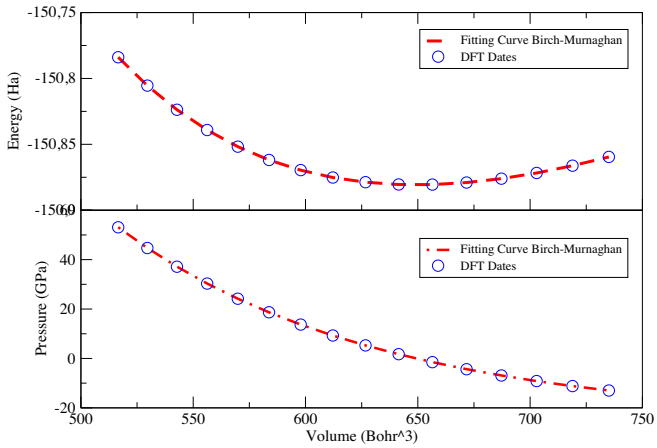

Fig. 3. Plots of energy vs. volume (upper curve); and pressure vs. volume (lower curve), for α-AlF_3. The blue dots represent the theoretical data obtained with DFT. The dashed red lines are the fitting curves with the Birch–Murnaghan equation of state. (For interpretation of reference to color in this figure legend, the reader is referred to the web version of this article.)

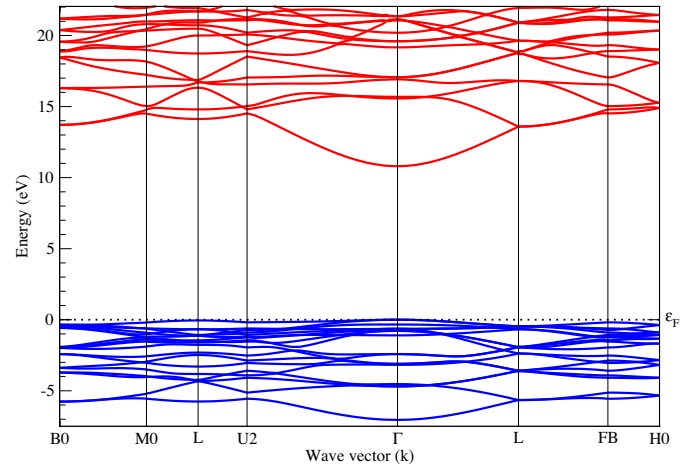

Fig. 4. Band Structure of α-AlF_3. This figure shows the band structure calculated with DFT, corrected with the GW method for the band gap, showing a direct band gap of 10.81 eV at the Γ point.

This fact does not represent a problem since AlF_3 is a chemically stable material [15]. In the right column inset we depict the Al2p XPS peak. For comparison, we added the positions of the same peak for AlF_3, Al_2O_3 and metallic aluminum. This result shows that neither the ex situ growth of the AlF_3 thin film, the electron bombardment have affected the electronic characteristics of the sample in a macroscopic way.

3.2. Electronic characterization

We used the method described by Birch and Murnaghan [16,17] to obtain the equilibrium lattice parameter from the calculated energy-pressure and energy–volume relationships.

The upper part of Fig. 3 shows the plot of total energy as a function of the volume, while the lower part of Fig. 3 shows the pressure as a function of the volume for α-AlF_3.

We carried out total energy calculations for different lattice parameters around the experimental value a_0, and by fitting the data to the equations of states of Birch–Murnaghan, we obtained the equilibrium volume V_0, the bulk modulus B_0, the pressure derivative of the bulk modulus B' and the minimum energy of the system E_0. Our structural calculations are sumarized in Table 1, together with other available results, which are only theoretical reports. The agreement is quite well, considering that the other calculations were done for the cubic phase.

Our DFT calculations were performed within the GGA approximation scheme for the exchange and correlation potential given by Perdew, Burke and Ernzerhof (PBE) [18], using norm conserving pseudopotentials for Al and F in the Troullier Martins scheme [19] which were obtained from the ABINIT package [20]. The eigenvalues and eigenfunctions of the Kohn–Sham [21,22] equations were solved self-consistently using a $12 \times 12 \times 12$ Monkhorst and Pack [23] grid to sample the Brillouin zone (BZ), including 40 bands, 24 of them are valence bands and are below the Fermi energy level E_F, and a 70 Ry cut-off energy for the wave functions. These parameters yielded a convergence of the total energy better than 2×10^{-5} Ry, and were used for the calculation of the densities of states, the band structure, the structural and the optical properties, and the EELS function. To the best of our knowledge, there are no previous experimental data on bulk modulus, optical spectra and EELS for α-AlF_3.

Fig. 4 shows the calculated electronic band structure along various symmetry points in the first BZ for α-AlF_3 using DFT with a GGA-PBE scheme for the exchange and correlation potential. While the band scheme and corresponding DOS give three well defined regions, in Figs. 4 and 5 the inner region is not shown since the bands are very deep and sharp, located between −21 and −19 eV approximately, and are not significant for our study. The following bunch of bands, form the valence region, which ranges between −7 eV up to the Fermi energy E_F. The next bunch of bands is the conduction band region, starting at 7.79 eV and up. This is the band gap obtained with the DFT-GGA-PBE scheme, which even with its known underestimation, indicates that α-AlF_3 is a direct band gap insulator at the Γ point. This result is in agreement with a previously reported result [7] within the DFT scheme for cubic AlF_3.

Table 1
DFT calculated results for structural parameters of α-AlF_3.

	Phase	V_0 (Bohr^3)	B_0 (GPa)	B'	E_0 (Ha)
This work	Rhomb	649.25	137	3.47	−150.88
PSP	Cubic	853.70[a]	146.6[a]		
FP-LAPW	Cubic	865.50[a]	150[a]		

[a] From Ref. [7].

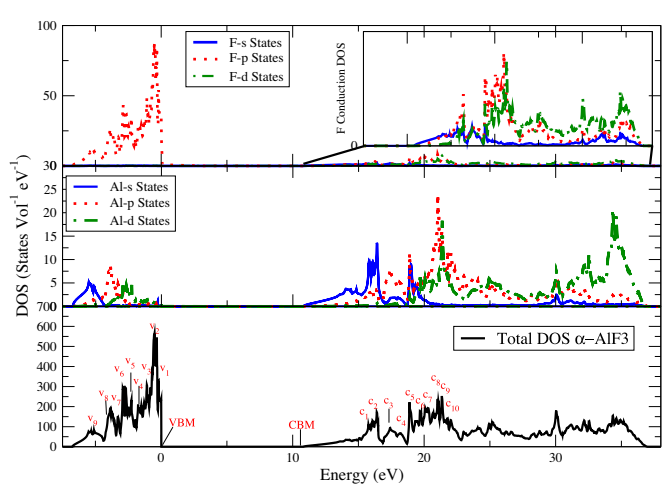

Fig. 5. Density of states of α-AlF_3. In the lower part we show the total density of states, at the center the Al PDOS is shown, and in the upper part we show the PDOS for the F-states. The inset of the upper level shows a zoom of the conduction zone. The band-gap shown is the calculated with the GW method.

To overcome the underestimation of the band gap that the ground state formulation of the DFT provides, we made further calculations including many body effects with the quasiparticle GW approximation proposed by Hedin [24]. In this formulation the self-energy of the electron–electron interaction is obtained as the screened coulomb interaction, W times the Green function propagator G. We used the calculation scheme proposed by Onida et al. [25], from which we obtained a band-gap in very good agreement with our experimental measurements. With this correction, we used a $10 \times 10 \times 10$ Monkhorst and Pack [23] grid to sample the first BZ, a 70 Ry cut-off energy and 48 bands for the Kohn Sham self consistent calculation, a lower cut-off energy for the expansion of the wave functions of 10 Ry, 8 Ry for the screening, and 14 Ry for the planewave set used to generate the exchange part of the self-energy operator. This set of parameters allowed a convergence of the GW corrections for the band gap better than 10 meV, obtaining a band gap of 10.81 eV at the Γ point in very good agreement with our experimental value of ~9.5 eV measured by ELLS, see Fig. 14, and the 10.8 eV value reported by Konig et al. [13].

Fig. 5 shows the DOS of α-AlF_3. In the lower part of the figure we depict the total DOS. In the middle part we show the partial density of states (PDOS) for Al states and finally the DOS for F states is described in the upper part. The inset represents a zoom of the conduction region of the F partial DOS. To facilitate the DOS discussion, the different peaks were named v_1 to v_8 for the valence region and c_1 to c_{10} for the conduction region, as is shown in the bottom of Fig. 5. In Table 2 we show the states and atoms that contribute to each peak, in decreasing order of contribution.

By comparing the band structure and the DOS (Figs. 4 and 5, respectively) we can make a broad analysis of the properties of the material. The structures of the total and partial DOS are located in the energy range from −22 eV to 32 eV approximately, with three dominant structures that are in coincidence with the regions of the band structure. The partial DOS give a useful picture of the principal contributions to the electronic structure, and the nature of the bonding. Starting from the core region, (not shown in Fig. 4), this has principal contribution from F-s orbitals and less contributions of Al-s, Al-p and Al-d orbitals. Likewise, the valence region has principal contributions of F-p states with a splitted peak close to the Fermi energy E_F. The lower region of the valence bands also have contributions from Al-s, Al-p and Al-d orbitals while the upper region is dominated by the F-p states. Thus, it can be seen that F-p states has a prominent role in the valence band edge of the material. Finally, the conduction region has main contributions from Al-s, Al-p and Al-d orbitals while the F orbitals made only a minor contribution to the DOS in this region, as it is shown in the inset of the upper part of Fig. 5 and in detail in Table 2.

Table 2
Relevant calculated DOS peaks (eV) and their contributing states for α-AlF_3. The orbitals are shown in decreasing order of contribution.

DOS peak	DOS energy	Contributing states	
		Main	Minor
V_8	−5.02	F-p	Al-s Al-p
V_7	−3.85	F-p	Al-p
V_6	−3.19	F-p	Al-p Al-d
V_5	−2.82	F-p	Al-p Al-d
V_4	−2.16	F-p	Al-d
V_3	−1.64	F-p	Al-d
V_2	−0.98	F-p	
V_1	−0.32	F-p	
VBM	0		
CMB	10.81		
C_1	14.15	Al-s Al-p	F-p
C_2	15.7	Al-s Al-p	F-p F-s
C_3	16.14	Al-s Al-p	F-p
C_4	16.43	Al-s F-p	Al-p
C_5	17.39	Al-p	Al-s
C_6	18.27	Al-p Al-s	F-p F-s
C_7	18.93	F-p Al-s	Al-s
C_8	19.74	Al-d Al-p	F-p
C_9	20.11	Al-p Al-d	F-p
C_{10}	21.09	Al-d Al-p	F-p

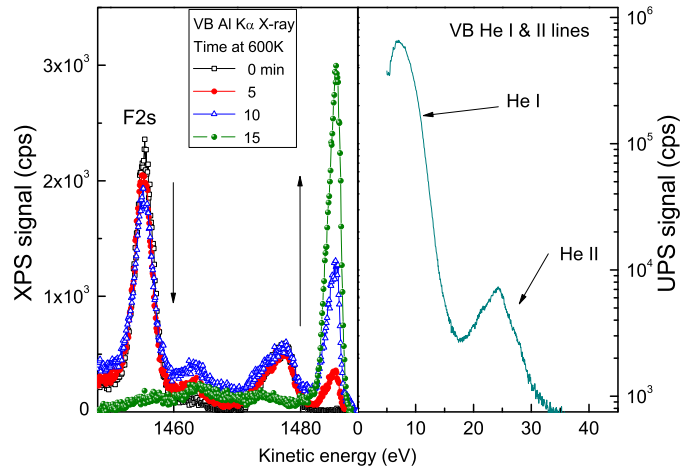

Fig. 6. Left column: Evolution of the AlF_3 on Cu valence band, and F 2s peak as the fluoride films is evaporated from the surface, excited by Al Kα line. Right column. AlF_3 on Cu, valence band taken with He I and II lines.

In Fig. 6 we show the photoelectron spectra, around the energy corresponding to the valence band, excited by Al Kα X-rays (left column) and He I and II UV photons (right column) corresponding to a thin film of AlF_3 on Cu. The spectra were not corrected for the background and they are depicted as a function of the kinetic energy.

In the left panel of Fig. 6 we can follow the desorption of the insulator film through the F2s photoelectron peak, as well as the modification of the valence band with the disappearance of the AlF_3 electron structure, around 1475 eV, and the appearance of the characteristic structure of 3d Cu states. On the right column we depict the electron emission excited by both UV lines of He. As the photoelectrons excited from the valence band by the He I line (21.2 eV) have relatively low energies it is difficult to separate their contribution to the total signal from the tail of the low secondary electrons. So it is clear from this experiment that useful information about the valence band electronic structure is better extracted from the higher energy He II line (40.8 eV) excitation. Also by looking at the different scales we can appreciate the different sensitivities of both techniques.

In Fig. 7 we compare experimental spectra with theoretical results. On the left panel we show valence band spectra obtained experimentally after a background correction of the spectra shown in Fig. 6. It can be readily seen that the spectra obtained with UPS and XPS are quite similar despite the big difference in the photon excitation energies used. In the right panel of Fig. 7 we compare the UPS valence band spectrum with the theoretical VB total DOS as it was shown at the bottom part of Fig. 5. We fitted the UPS spectrum with three gaussians and noticed that the position of two of them (the two with lower binding energy) agrees roughly with the position of peaks in the theoretical DOS. However the amplitudes of these peaks are different, and this effect could be ascribed to the fact that we are not taking into account the excitation cross section to correct the UPS spectrum.

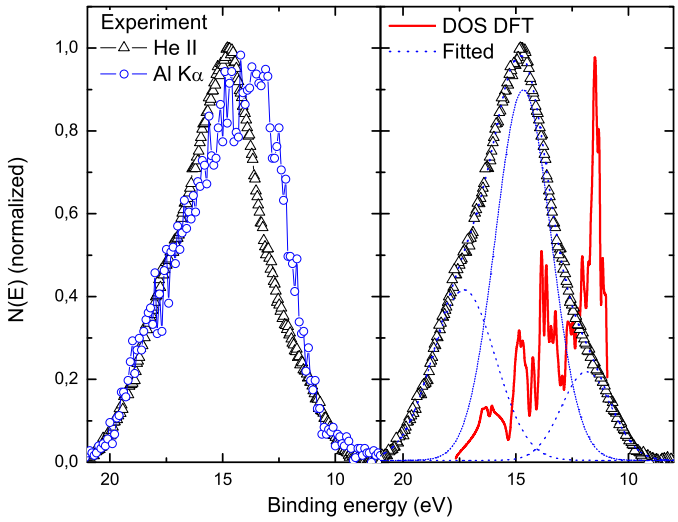

Fig. 7. Left panel: experimental valence band spectra obtained with UPS and XPS after background subtraction. Right panel: comparative plot of the UPS VB spectrum and the calculated one.

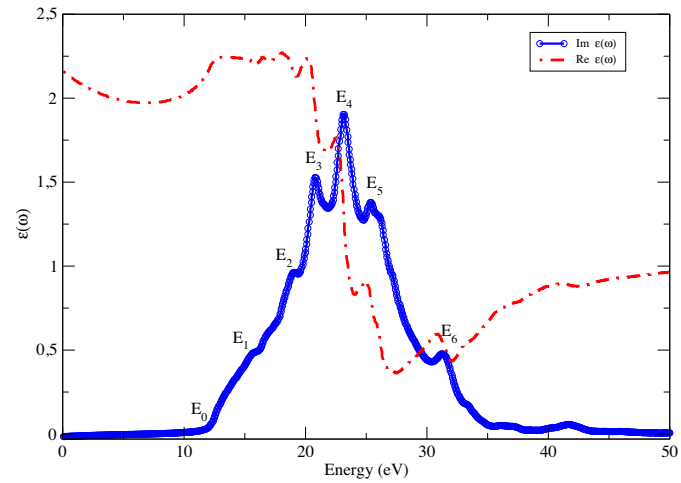

Fig. 8. Plots of the real part $\varepsilon_1(\omega)$ (dashed lines) and imaginary part $\varepsilon_2(\omega)$ (solid lines) of the dielectric function calculated with DFT.

3.3. Optical properties

From the DOS and the interband momentum matrix elements, the imaginary part of the dielectric function $\varepsilon_2(\omega)$ can be calculated as [26]:

$$\varepsilon_2(\omega) = \frac{Ve^2}{2\pi\hbar m^2\omega}\int d^3\vec{k}\sum_{nn'}|\langle\vec{k}n|\vec{p}|\vec{k}n'\rangle|^2 f(\vec{k}n)^*(1-f(kn')) \times\delta(E_{\vec{k}n}-E_{\vec{k}n'}-\hbar\omega) \quad (1)$$

where $\vec{p}$ is the momentum operator, $|\vec{k}n\rangle$ is the eigenfunction with eigenvalue $E_{\vec{k}n}$, n and n' are the band index and $f(\vec{k}n')$ and $f(\vec{k}n)$ are the occupation numbers of the n'th and n bands at the k point. The integral is over the first BZ. The real part of the dielectric function $\varepsilon_1(\omega)$ is directly obtained from $\varepsilon_2(\omega)$ by using the Kramers and Kronig relationships [26],

$$\varepsilon_1(\omega) = 1 + \frac{2}{\pi}P\int_0^\infty \frac{\varepsilon_2(\omega)\omega' d\omega'}{\omega'^2-\omega^2} \quad (2)$$

were P means the principal value of the integral.

Other optical constants as the refractive index $n(\omega)$, the extinction coefficient $K(\omega)$, the reflectivity at normal incidence $R(\omega)$, and the electron energy loss EELS, can be obtained from the dielectric function through the following relations: [26]

$$n(\omega) = \sqrt{\frac{|\varepsilon(\omega)| + \varepsilon_1(\omega)}{2}} \quad (3)$$

$$K(\omega) = \sqrt{\frac{|\varepsilon(\omega)| - \varepsilon_1(\omega)}{2}} \quad (4)$$

$$R(\omega) = \frac{(n-1)^2 + k^2}{(n+1)^2 + k^2} \quad (5)$$

$$\alpha(\omega) = \frac{2\omega}{c}\left(\frac{|\varepsilon(\omega)| - \varepsilon_1(\omega)}{2}\right)^{1/2} \quad (6)$$

$$EELS(\omega) = Im\left\{-\frac{1}{\varepsilon(\omega)}\right\} \quad (7)$$

Since the optical spectra calculations usually require large dense meshes, we maintained the described parameters used for the ground state DFT calculation to solve the Kohn and Sham matrix (KS), while testing the convergence of the optical calculations for meshes of $21 \times 21 \times 21$, $23 \times 23 \times 23$ and $25 \times 25 \times 25$ k points, finding the same spectra with the three meshes. In the same way, we did energy convergence tests, finding that increasing the range up to 50 bands with the k-meshes, established the curves of optical functions, as well as the EELS spectra. Then we adopted the $23 \times 23 \times 23$ k-point sampling in the first BZ, including 50 bands, from which we obtained the dielectric constant $\epsilon(\omega = 0)$,the real and imaginary parts of dielectric function $\epsilon_1(\omega)$ and $\epsilon_2(\omega)$, and the EELS function. Fig. 8 shows the imaginary and real part of the dielectric function for α-AlF_3, while the EELS function is presented in Fig. 12. From the solid lines of Fig. 8, it is evident that the material has a main absorption peak E_4 at 25 eV approximately. The curve has a bell shape, starts with a slight increase, has a principal peak E_4 at 25 eV and two small shoulders at 19 eV and 22 eV. After the main peak the curve starts to decrease showing two peaks, E_5 at 27 eV, and E_6 at 32 eV. From the imaginary part of the dielectric function, and applying the Kramers–Kronig relationships we got the real part of the dielectric function $\varepsilon_1(\omega)$ as shown by the dashed line of Fig. 8. We obtained the dielectric constant ε_0 of 1.92 and 2.0 without local field effects. This fact, and the low dispersion presented by the upper part of the valence bands and the lower part of the conduction bands, (see Fig. 4), suggested to take into account the electron–hole interaction in the band gap region. We discuss the contribution of this interaction below.

In Fig. 9 we plotted with solid line the refractive index $n(\omega)$ obtained from the dielectric function using Eq. (3). Our results are in good agreement with measurements reported by Chindaudom and Vedam [27], who measured the refractive index on AlF_3 and other fluoride materials by elipsometric techniques, reporting a value of $n = 1.4$ in the energy range between 300 nm and 700 nm. The dashed line of Fig. 9, represent the extinction coefficient $K(\omega)$ calculated using Eq. (4). In Fig. 10 we show the reflectivity $R(\omega)$ at normal incidence, obtained through Eq. (5) and in Fig. 11 the absorption coefficient of α-AlF_3 $\alpha(\omega)$ obtained from Eq. (6). Finally, Fig. 12 shows the calculated Electron Energy Loss Spectra, $EELS(\omega)$ obtained with Eq. (7).

By looking at Fig. 8, it is seen that the highest anisotropy in $\varepsilon_2(\omega)$ (solid line) occurs, approximately, in the 23–26 eV range, in agreement with the main peaks of the absorption coefficient as shown in Fig. 11. Tables 2 and 3 are helpful to track down the origin of all the peaks in the imaginary part of the dielectric function, related to the DOS and therefore with the orbital-states causing them. For example, peak E_1 at (17.36 eV) could be assigned to a

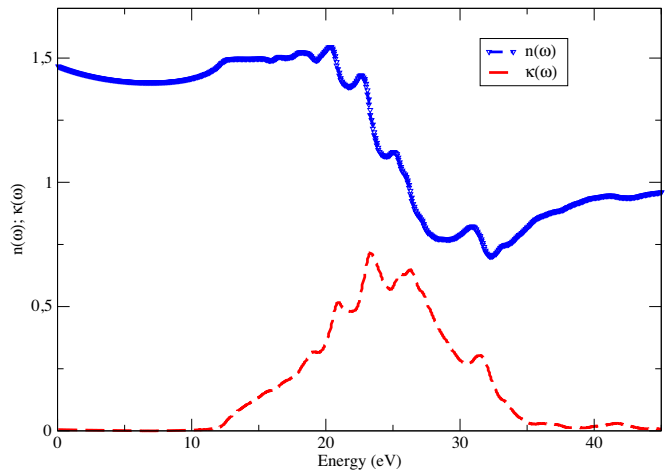

Fig. 9. Plots of the refractive index $n(\omega)$, solid lines, and extinction coefficient $K(\omega)$ dashed lines, for α-AlF_3.

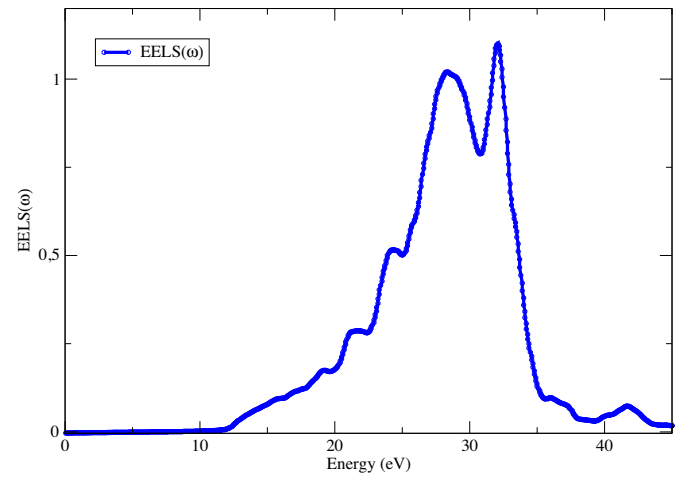

Fig. 12. Plot of the energy electron loss spectra $EELS(\omega)$ for α-AlF_3.

transition $V_2 \rightarrow C_3$, mainly due to F-p orbitals on the valence bands to Al-s and Al-p orbitals in the conduction band.

In ordered to consider the presence of excitonic effects in the band gap region, we included the electron–hole interaction through the Bethe–Salpeter Equation (BSE) [28], which uses two particle Green's functions that describes the electron-hole coupling and its propagation. The ab initio procedure that we used to solve the BSE was proposed by Onida et al. [25], and consists of three steps: (i) a ground state DFT calculation to obtain the eigenvalues of Kohn and Sham matrix (KS), (ii) a GW calculation to correct the KS eigenvalues of step (i), and (iii) the solution of the BSE considering the GW eigenvalues, KS orbitals and the screening of the electron–hole interaction. To develop this procedure we used a 14 × 14 × 14 Monkhorst and Pack [23] grid to sample the BZ, including 48 bands, and calculating the BSE correction between the bands 18 and 26 with a cut-off energy for the plane wave expansion of 12 Ry and 10 Ry for the screening. Fig. 13 shows the real $\varepsilon_1(\omega)$ and imaginary $\varepsilon_2(\omega)$ parts of the dielectric function, calculated with the excitonic effects through the BSE. This figure shows that the imaginary part $\varepsilon_2(\omega)$ have a main peak at approximately 11 eV and some small peaks in an energy range between 12 and 13 eV.

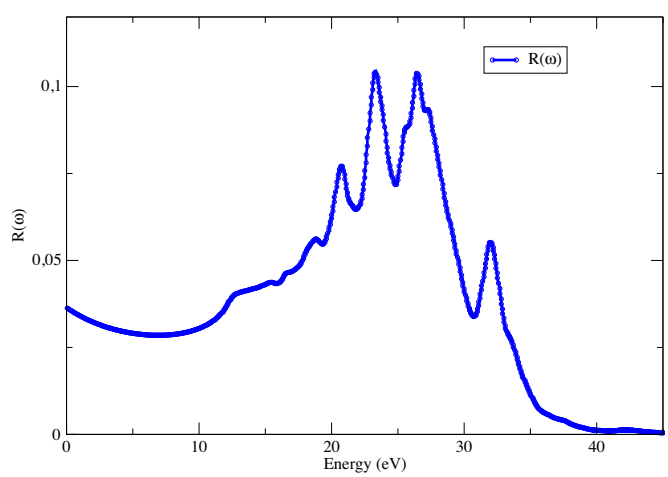

Fig. 10. Plot of the reflectivity at normal incidence $R(\omega)$ for α-AlF_3.

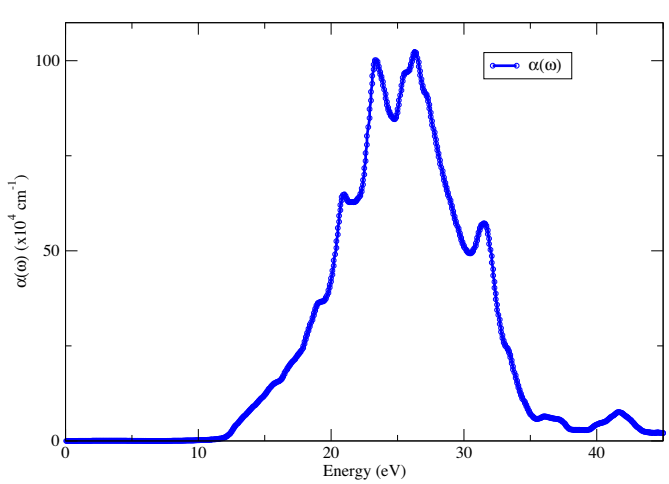

Fig. 11. Plot of the absorption coefficient $\alpha(\omega)$ for α-AlF_3.

3.4. EELS spectra

In the left panel of Fig. 14 we depict the energy loss spectra of metallic Cu and AlF_3, obtained from reflected low energy electrons.

Table 3
Imaginary part of the complex dielectric function of α-AlF_3 and its relationship with DOS. Energies are in eV.

DOS		ε_{2xx}		ε_{2yy}		ε_{2zz}	
Transition	Energy	Peak	Energy	Peak	Energy	Peak	Energy
		E_0	11.73	E_0	11.73	E_0	11.73
$V_1 \rightarrow CMB$	11.14	E_0	11.73	E_0	11.73	E_0	11.73
$V_2 \rightarrow CMB$	11.8	E_0	11.73	E_0	11.73	E_0	11.73
$V_1 \rightarrow C_5$	17.71	E_1	17.12	E_1	17.12	E_1	17.12
$V_2 \rightarrow C_3$	17.12	E_1	17.12	E_1	17.12	E_1	17.12
$V_3 \rightarrow C_3$	17.34	E_1	17.12	E_1	17.12	E_1	17.12
$V_2 \rightarrow C_6$	19.25	E_2	19.12	E_2	19.12	E_2	19.12
$V_3 \rightarrow C_5$	19.03	E_2	19.12	E_2	19.12	E_2	19.12
$V_3 \rightarrow C_6$	19.91	E_2	19.12	E_2	19.12	E_2	19.12
$V_4 \rightarrow C_5$	19.55	E_2	19.12	E_2	19.12	E_2	19.12
$V_5 \rightarrow C_4$	19.25	E_2	19.12	E_2	19.12	E_2	19.12
$V_6 \rightarrow C_{10}$	24.28	E_3	24.25	E_3	23.89	E_3	24.08
$V_7 \rightarrow C_{10}$	24.94	E_3	24.25	E_3	23.89	E_3	24.08
$V_8 \rightarrow C_8$	24.76	E_3	24.25	E_3	23.89	E_3	24.08
$V_5 \rightarrow C_{10}$	23.91	E_3	24.25	E_3	23.89	E_3	24.08
$V_8 \rightarrow C_{10}$	26.11	E_4	26.22	E_4	25.43	E_4	25.58
$V_8 \rightarrow C_9$	25.13	E_4	26.22	E_4	25.43	E_4	25.58

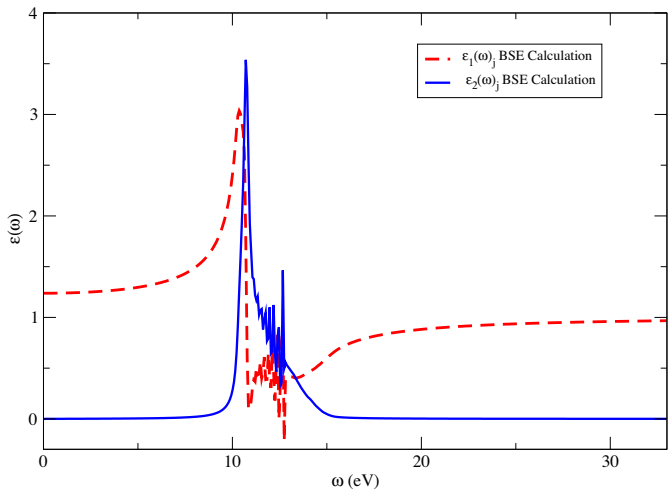

Fig. 13. Plots of the imaginary $\varepsilon_2(\omega)$, solid line, and real $\varepsilon_1(\omega)$ part, dotted line, of dielectric function for α-AlF_3, calculated with the BSE theory including the electron–hole interaction.

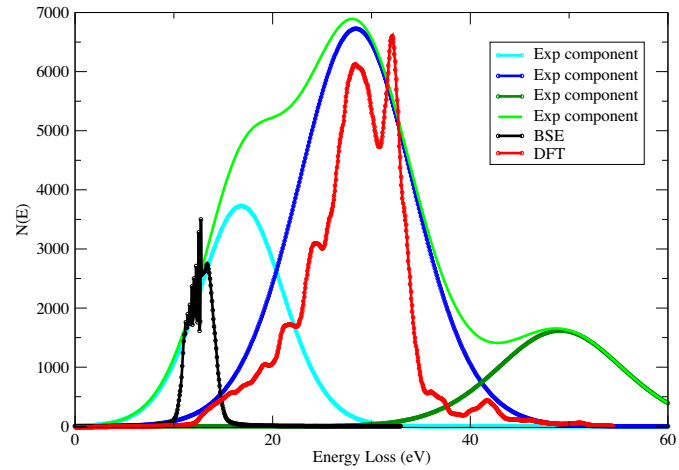

Fig. 15. Experimental and theoretical curves of electron energy loss for Cu–AlF_3. The experimental curve (green line) corresponds to the inelastic losses of the F 1s XPS peak and it has been deconvoluted into three components (cian, blue and dark green lines). Theoretical curves (black an red lines) were obtained by BSE (dark line) and DFT calculations respectively red line. (For interpretation of reference to color in this figure legend, the reader is referred to the web version of this article.)

These spectra show the plasmon losses that correspond to Cu and the band gap of the insulator film. In the right panel we show the F 1s photoelectron peak including the energy loss part of the spectrum. We observe the good correlation between these measurements in spite of the different experimental assemblies. Reflected low energy electrons were measured with a CMA in the fixed retarding ratio mode (FRR) while the F 1s XPS peak (at 800 eV) was measured in the fixed analyzer transmission mode (FAT) with a hemispherical analyzer. The larger background observed for Cu is due to its metallic nature. On the other hand, the numerical values obtained for the Cu plasmon (~7.5 eV) and the AlF_3 gap (~9.5 eV) are in good agreement with previous measurements [13].

In Fig. 15 we compare experimental and theoretical results for EELS. We show how the electron energy loss structure of the F 1s XPS peak can be deconvoluted into three components (cyan and green lines), after the background has been removed. The higher energy experimental dark green curve centered at about 50 eV, that might come from the excitation of a inner state, was not taken into account in the theoretical model to keep the calculations feasible.

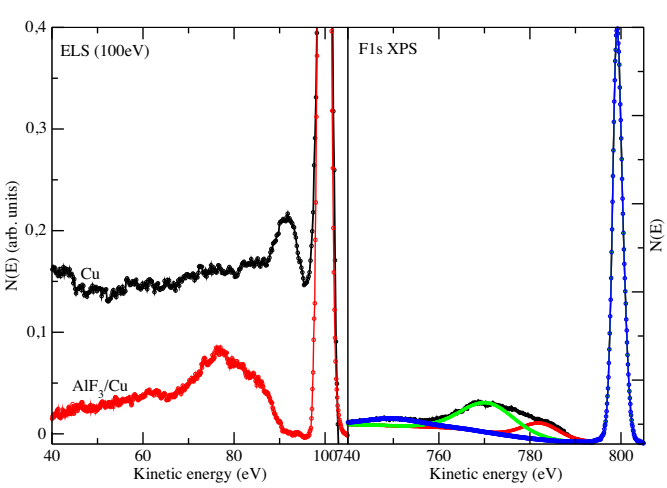

Fig. 14. Left: electron energy loss of Cu and AlF_3 obtained with 100 eV impining electrons. Right: F 1s photoelectron spectrum obtained with Mg Kα line. The spectrum was extended to include the energy loss features.

We also show the two components forming the theoretical EELS curve: (i) the solid red line is the contribution coming from the DFT calculation. This contribution compares well with the experimental curve corresponding to the main peak of the spectrum which is in the region of about 20–40 eV and with its principal value at 28 eV; (ii) solid black line is the contribution due to excitonic effects calculated using the Bethe–Salpeter equation. The agreement between the position and left flank of the DFT and BSE peaks is rather good when compared to the low energy components of the experimental EELS. Even when the experimental EELS components around the band gap region are wider than the calculated excitons, it is valuable that their main features can be explained theoretically by taking into account the electron–hole interaction through the BSE approximation in the calculation of optical properties.

4. Conclusion

We report what to the best of our knowledge is the first ab initio study on the structural, electronic and optical properties of bulk α-AlF_3, extended by including many body effects through the GW approximation for the band gap, and the excitonic effects through the BSE theory for the optical spectra. We have obtained a very good agreement between the experimental band-gap of ~9.5 eV, and the calculated with the GW approximation, a direct band-gap of 10.81 eV in the Γ point. We calculated the value of the dielectric constant ε_0 of 1.92 eV. We compared theoretical results of DOS and EELS with the XPS, UPS and EELS experiments showing that the main experimental EELS features can be explained using our theoretical formulations. In particular we showed through the use of the BSE calculations, that excitonic effects coming from the electron-hole interaction, can explain the low energy component around the band-gap energy region obtained in the experimental EELS.

Acknowledgements

The authors acknowledge financial support from Consejo Nacional de Investigaciones Científicas y Técnicas (CONICET), Agencia Nacional de Promoción Científica y Tecnológica (ANPCyT), Universidad Nacional de Entre Ríos (UNER) and Universidad Nacional del Litoral (UNL).

References

[1] A. Wander, C.L. Bailey, S. Mukhopadhyay, B.G. Searle, N.M. Harrison, Ab initio studies of aluminium fluoride surfaces, J. Mater. Chem. 16 (2006) 1906–1910.
[2] C.L. Bailey, S. Mukhopadhyay, A. Wander, B.G. Searle, N.M. Harrison, First principles characterisation of aluminium trifluoride catalysts, J. Phys. Conf. Ser. 117 (2008) 1906–1910.
[3] L.I. Vergara, R. Vidal, J. Ferron, Electron induced reduction on AlF_3 thin film, Appl. Surf. Sci. 229 (2004) 301.
[4] C. Ma, Y. Berta, Z.L. Wang, Patterned aluminum nanowires produced by electron beam at the surfaces of AlF_3 single crystals, Solid State Commun. 129 (2004) 681.
[5] R. Konig, G. Scholz, K. Scheurell, D. Heidemann, I. Buchem, W.E. Unger, E. Kemnitz, Spectroscopic characterization of crystalline AlF_3 phases, J. Fluorine Chem. 131 (2010) 91.
[6] P. Daniel, A. Bolou, M. Rousseau, J. Nouet, J.L. Fourquet, M. Leblanc, R. Burriel, A study of the structural phase transitions in AlF_3: X-ray powder diffraction, differential scanning calorimetry (DSC) and Raman scattering investigations of the lattice dynamics and phonon spectrum, J. Phys.: Condens. Matter 2 (1990) 5663.
[7] Y.R. Chen, V. Perebeinos, P.B. Allen, Density-functional study of the cubic-to-rhombohedral transition in α-AlF_3, Phys. Rev. B. 69 (2004) 054109.
[8] P. Chupas, M. Ciraolo, J. Hanson, C. Grey, In situ X-ray diffraction and solid-state NMR study of the fluorination of -Al_2O_3 with HCF_2Cl, J. Am. Chem. Soc. 123 (2001) 1694.
[9] A. Kokalj, Computer graphics and graphical user interfaces as tools in simulations of matter at the atomic scale, Comput. Mater. Sci. 28 (2003) 155.
[10] M. Lax, Symmetry Principles in Solid State and Molecular Physics, 1974, p. 451, Fig E4(b), Dover.
[11] A. Le Bail, F. Calvayrac, Hypothetical AlF_3 crystal structures, J. Solid State Chem. 179 (2006) 3159.
[12] J.C. Moreno-López, R. Vidal, M.C.G. Passeggi, J. Ferrón, STM study of the initial stages of AlF_3 on Cu(100), Phys. Rev. B. 81 (2010) 075420.
[13] D. Konig, R. Scholz, D. Zahn, G. Ebest, Band diagram of the $AlF_3/SiO_2/Si$ system, J.Appl. Phys. 97 (2005) 093707.
[14] Standard Reference Database;1; 20, Version 4.1, http://srdata.nist.gov/xps/Default.aspx.
[15] G. Ruano, J.C. Moreno-López, M.C.G. Passegi Jr., R. Vidal, J. Ferrón, M.A. Nino, R. Miranda, J.J. de Miguel, Morphology and thermal stability of AlF_3 thin films grown on Cu(100), Surf. Sci. 606 (2012) 573.
[16] F. Birch, Finite Elastic Strain of Cubic Crystals, Phys. Rev. 71 (1947) 809.
[17] F.D. Murnaghan, The compressibility of media under extreme pressures, Am. J. Math. 49 (1937) 235.
[18] J.P. Perdew, K. Burke, M. Ernzerhof, Generalized gradient approximation made simple John, Phys. Rev. Lett. 77 (1996) 3865.
[19] N. Troullier, J.L. Martins, Efficient pseudopotentials for plane-wave calculations, Phys. Rev. B. 43 (1991) 1993.
[20] X. Gonze, B. Amadon, P.M. Anglade, J.M. Beuken, F. Bottin, P. Boulanger, F. Bruneval, D. Caliste, R. Caracas, M. Cote, T. Deutsch, L. Genovese, Ghosez Ph, M. Giantomassi, S. Goedecker, D. Hamann, P. Hermet, F. Jollet, G. Jomard, S. Leroux, M. Mancini, S. Mazevet, M.J.T. Oliveira, G. Onida, Y. Pouillon, T. Rangel, G.M. Rignanese, D. Sangalli, R. Shaltaf, M. Torrent, M.J. Verstraete, G. Zrah, J.W. Zwanziger, Comput. Phys. Commun. 180 (2009) 2582.
[21] W. Kohn, L.J. Sham, Self consistent equations including exchange and correlation effects, Phys. Rev. 140 (1965) 1133.
[22] P. Hohenberg, W. Kohn, Inhomogeneous electron gas, Phys. Rev. 136 (1964) 864.
[23] H.J. Monkhorst, J.D. Pack, Phys. Rev. B 13 (1976) 5188.
[24] L. Hedin, New method for calculating the one-particle Green's function with application to the electron-gas problem, Phys. Rev. 139 (1965) 796.
[25] G. Onida, L. Reining, R.W. Godby, R. DelSole, W. Andreoni, Ab initio calculations of the quasiparticle and absorption spectra of clusters: the sodium tetramer, Phys. Rev. Lett. 75 (1995) 818.
[26] P.Y. Yu, M. Cardona, Fundamentals of Semiconductors Physics and Materials properties, Springer, Boston, MA, United States, 2010.
[27] P. Chindaudom, K. Vedam, Studies on inhomogeneous transparent optical coatings on transparent substrates by spectroscopic ellipsometry, Thin Solids Films 234 (1993) 439.
[28] E.E. Salpeter, H.A. Bethe, A relativistic equation for bound-state problems, Phys. Rev. 84 (1951) 1232.